buildings

MDPI

Article

The Inclusion and Initial Damage Inspection of Intelligent Cementitious Materials Containing Graphene Using Electrical Resistivity Tomography (ERT)

Shijun Wang [1,2], Shengjiang Peng [1,3], Qiong Liu [4,*] and Wanwei Li [1]

[1] Gansu Electric Power Corp., State Grid, Lanzhou 730030, China; angelofkill@126.com (S.W.); pshj@sina.com (S.P.); liwanw@gs.sgcc.com.cn (W.L.)
[2] School of Civil Engineering, Southeast University, Nanjing 210018, China
[3] School of Economics and Management, North China Electric Power University, Beijing 102206, China
[4] School of Environment and Architecture, University of Shanghai for Science and Technology, Shanghai 200093, China
* Correspondence: lq612@usst.edu.cn; Tel.: +86-13301997237

Abstract: This paper examines the theoretical foundations of electrical resistivity tomography (ERT) technology, followed by the finite element analysis method, for the positive problem and the linear back-projection (LBP) procedure for the inverse problem. The conductivity distribution image of the modeled concrete is then reconstructed, which includes one circular aggregate and the surrounding mortar. It is discovered that the conductivity obtained can be used to find the inclusive aggregate, mortar, and interfacial transition zone (ITZ). Natural aggregate and mortar have conductivities of 0.046 ms/cm and 0.115 ms/cm, respectively. Additionally, the conductivity of the ITZ, which is always regarded as the initial damage, is about 0.081 ms/cm. ERT is a cost-effective and readily available technique for determining the initial distribution of the aggregate and related ITZ. Therefore, ERT is a promising tool for determining inclusions and initial damage in concrete.

Keywords: smart concrete; graphene; electrical resistivity tomography; ITZ; inclusion

check for updates

Citation: Wang, S.; Peng, S.; Liu, Q.; Li, W. The Inclusion and Initial Damage Inspection of Intelligent Cementitious Materials Containing Graphene Using Electrical Resistivity Tomography (ERT). *Buildings* **2024**, *14*, 2098. https://doi.org/10.3390/buildings14072098

Academic Editor: Bjorn Birgisson

Received: 1 April 2024
Revised: 2 June 2024
Accepted: 2 July 2024
Published: 9 July 2024

Copyright: © 2024 by the authors. Licensee MDPI, Basel, Switzerland. This article is an open access article distributed under the terms and conditions of the Creative Commons Attribution (CC BY) license (https://creativecommons.org/licenses/by/4.0/).

1. Introduction

Concrete is the most widely used material in infrastructure due to its great compressive strength and formability. The health of concrete structures should be monitored to ensure their safe operation and upkeep, especially for some crucial structural joints. Researchers have had interest in structural health monitoring [1]. Resistance strain gauges, piezoresistive ceramic sensors, and optical fiber sensors are the traditional sensors used in concrete structures. However, these techniques have limitations, such as a short service life or incompatibility with structural concrete [2]. During the last two decades, intrinsically self-induced concrete has achieved great success [3].

Water-soluble hydration products and ions impurities such as $Ca(OH)_2$ are dissolved in ordinary concrete. The ionization process produces freely moving anions in the pore water, which function as carriers for concrete conductivity [4]. Regarding the damage evolution mechanisms of loading, corrosion, and leaching, micropores and cracks are the perpetrators. As a result, the electrical properties of concrete are closely related to its pore structure and damage development [5]. The internal porosity and damage growth of concrete may be determined by assessing its electrical conductivity, giving a theoretical possibility for the nondestructive detection of the distribution characteristics of the initial damage and damage evolution in concrete [6,7].

Although the movement of anions causes the possibility of damage detection in normal concrete, it has limited electrical conductivity which also limits accurate and sensitive damage measurement. In its dry state, concrete has a resistivity of 10^5–10^9 Ω·m. When

conductive fillers such as carbon fiber, carbon powder, graphite powder, steel fiber, or graphene are introduced into concrete, the conductivity of concrete increases proportionate to the content of the conductive fillers [8,9]. When the content exceeds a certain threshold, the concrete gains a semiconductor state and the pressure-sensitive characteristics of intelligence, which can illustrate the damage to the concrete [10,11].

Many researchers have engaged in the application of electrical resistivity tomography (ERT). IA model for a liquid/solid mixing process using ERT was validated [12]. ERT was also utilized to detect solid matter settling in a vertical pipeline hydraulic transmission system [13]. ERT was utilized to identify geological settings [14] and to study seawater intrusion's extent and geometric characteristics in an eastern Greek bay's coastal aquifer [15]. It was demonstrated that the application of ERT could follow the evolution of water distribution in concrete structures over time [16]. A recent study illustrated that ERT can be used to visualize the distribution of resistivities to show the chloride content in civil engineering structures [17]. Research has increasingly begun to focus on nondestructive monitoring methods to provide a better diagnosis of the service life of reinforced concrete structures [18]. A wide range of theories of inverse problem solving have been summarized, including linear back-projection (LBP), the Gauss–Newton method, Bayesian filtering, and so on. Among them, the LBP method is commonly used in commercial software due to its fast calculation and acceptable reconstruction image accuracy [19].

ERT was also used to detect inclusions and cracks in concrete. Specially designed concrete specimens were cast containing square and circular inclusions, as well as cracks made of varied lengths of plastic sheets. The results showed that ERT can detect inclusions of different shapes and cracks of different sizes [20]. A similar experimental study was conducted with a thin layer of electrically conductive material painted on the surface of a concrete sample. It could be used as a sensing skin to detect and locate cracking and damage in the concrete substrate [21]. Another study designed a 4.6 × 3.7 m concrete plate at a construction site for shrinkage crack detection, and the results showed that ERT could be used for macroscopic scale crack detection [22,23]. A recent study developed analytical solutions and conducted experimental validation on cement mortar samples with simulated cracks. The measurement method, among other configurations, demonstrated faster and higher sensitivity in detecting inclusions at greater depths [24]. A large-scale application of self-sensing concrete in airport runway pavements illustrated that ERT can be used to characterize spatially distributed damage during accelerated pavement testing [25]. Another study achieved high-accuracy rebar position detection using a deep-learning-based electrical resistivity tomography (ERT) technique [26]. In addition to mechanical damage detection, resistivity profiles can also be converted to chloride profiles, which are similar to those assessed using regular methods [27,28]. A newly developed convolutional neural network (a deep learning method) model successfully distinguished rebar position in concrete from ERT images [29].

Although ERT has been employed in several fields, it has rarely been used to assess the health of concrete, not only because concrete, called cementitious composite, contains aggregates but also because the aggregates and surrounding mortar have varied resistivities. This study conducted an ERT test for a modeled concrete with the finite element analysis technique for the forward problem and the LBP algorithm for the inverse problem. Following the experimental test, ERT reconstructed the conductivity tomography of the modeled concrete with the measured voltages. The novelty of this study is reflected in the fact that the model concrete used reflects the exact position and shape of the included aggregate, as well as the distribution of ITZ, which makes it convenient to verify the correctness of the analysis results of ERT with the LBP method. The reconstruction of each phase of the specimen sheds light on the feasibility of utilizing ERT to identify the aggregate and related ITZ, which have varied conductivities as to the mortar matrix. This investigation highlights the potential of ERT as a valuable tool for the tomographic imaging of the inclusions and initial damages of concrete.

2. Materials and Methods

2.1. Materials

P.O. 52.5 Portland cement (chemical composition is shown in Table 1) was adopted for casting the specimens conforming to Chinese code (GB 175-2020) [30]. The sand used in this study was normal river sand, and potable water was used for mixing. A polycarboxylate-based superplasticizer was used to assist in dispersing the graphene into water together with an ultrasonic treatment. As an additional conductive substance, graphene was employed; the fundamental characteristics of graphene can be seen in Table 2. To make the modeled concrete, a circular inclusive of marble was prepared.

Table 1. Chemical composition of cement (w/%).

Cao	Si_2O	MgO	SO_3	Al_2O_3	K_2O	Na_2O	Fe_2O_3	Ignition Loss
63.80	20.78	1.50	2.02	4.57	0.65	0.23	5.12	1.31

Table 2. Physical properties of graphene nano-platelets used in the test.

Size	Density (kg/m^3)	Specific Surface Area (m^2/g)	Appearance
In-plane diameter: 5–15 μm; Thickness: 2–3 nm	1400	190	Dark powder

The mix proportion of the mortar is illustrated in Table 3, from which the water/cement ratio is shown to be 0.6, and the graphene content is 6.4% of the cement by weight. The weight of the superplasticizer was the same as that of the graphene.

Table 3. Mix proportion (g).

Cement	Water	Sand	Graphene	Superplasticizer
100	60	300	6.4	6.4

2.2. Samples

To equally spread graphene in concrete, it was required to first disperse the graphene in water. Graphene nanoparticles were distributed in water by using an ultrasonic treatment and a polycarboxylate superplasticizer as the surfactant. Figure 1 illustrates the experimental procedure. Water, graphene, and polycarboxylate superplasticizer were added into a beaker in the stated proportions. The beaker was then placed in the ultrasonic dispersing machine with a power of 400 W for 30 min, as illustrated in the first step in Figure 1. The mixture was continuously agitated with a stirring rod to avoid precipitation in the beaker during the ultrasonic dispersion. After 30 s of mixing the dry sand and cement, the graphene suspension was introduced during the continuous mixing process. Another 30 s of slow mixing followed by 30 s of fast mixing prepared the conductive mortar for casting.

The cylindrical mortar sample was cast with a diameter of 100 mm and a thickness of 20 mm. A circular inclusive of marble was placed in the middle of the mold, and then the intelligent mortar was poured around it to make the modeled concrete, as illustrated in the third stage in Figure 1. In addition, a contrast specimen was also prepared without the inclusion (Figure 2a). After three minutes on the vibration table, the specimens were put in a normal curing chamber for 28 days.



Figure 1. Experiment schedule.

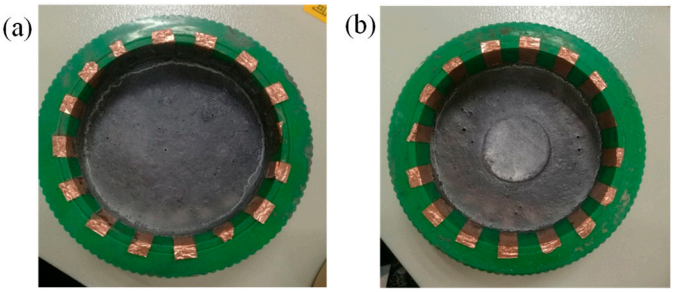


Figure 2. Samples for ERT: (**a**) contrast, (**b**) modeled concrete.

The contact electrode was made of copper foil. There were 16 electrodes whose width was 10 mm, and they were equally placed around the cylindrical specimen. The sensitive field electrode array surrounded the cylindrical specimen. The electrode array was linked to the excitation unit, which applied excitation current to the specimen. The data collection system completed the signal acquisition. A schematic diagram of the electrode array is presented in Figure 2, which comprises two samples, one of which is the contrast mortar sample (Figure 2a) and the other is the modeled concrete sample (Figure 2b). The contrast sample had a relatively uniform conductivity, which was used to establish the finite elements and the relationship between the potential in the sensitive field and the electrodes. The modeled concrete was the specimen that contained an inclusion of low-conductivity marble.

2.3. Test Method

The excitation mode of an ERT system is classified into different categories based on the excitation source, the number of excitation hits, and so on. In this study, the ERT equipment from "Industrial Measurement Solutions (ITS)" company (Manchester, UK) was used, and the adjacent technique was adopted, which implied that two adjacent electrodes were injected with a current signal, and the collected voltage signal was positioned on

two other adjacent electrodes. For instance, when the injected electrodes were 1–2, the electrodes' coordinate serial numbers of the excitation source were 3–4, 4–5, . . ., 15–16, as shown in Figure 3. As a result, 208 border voltage readings were gathered, and only 104 voltage values were independent because the voltage-measuring electrode and the current-measuring electrode were symmetrical.

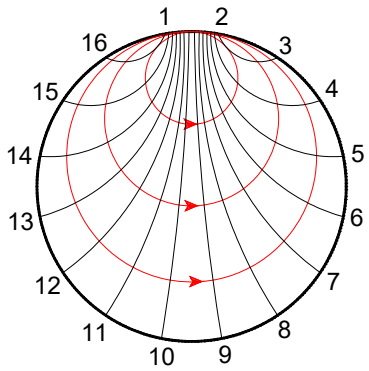


Figure 3. Electrodes and possible equipotential lines.

The contrast specimen was connected to the system to carry out the calibration first in order to generate a projection domain isoline coverage matrix to determine the isometric line area corresponding to each element. Then, the modeled concrete specimen was connected to the system, and the boundary voltages were collected according to the above rule.

3. Results

3.1. Inverse Problem Analysis

The inverse problem was solved using the LBP technique, based on the fact that the sensitive field is a hard field. The change in dielectric conductivity in the sensitive field did not affect the distribution of the sensitive field. The quadrilateral finite element approach was used; that is, the specimen was split into regular squares, having 316 elements in total (see Figure 4a). The element's grid division form was symmetrical, and each element was a conventional square element, making computation easy. According to the experiment's imaging results, this grid division form essentially satisfied the requirements of conductivity image reconstruction. The specific process of the LBP is as follows:

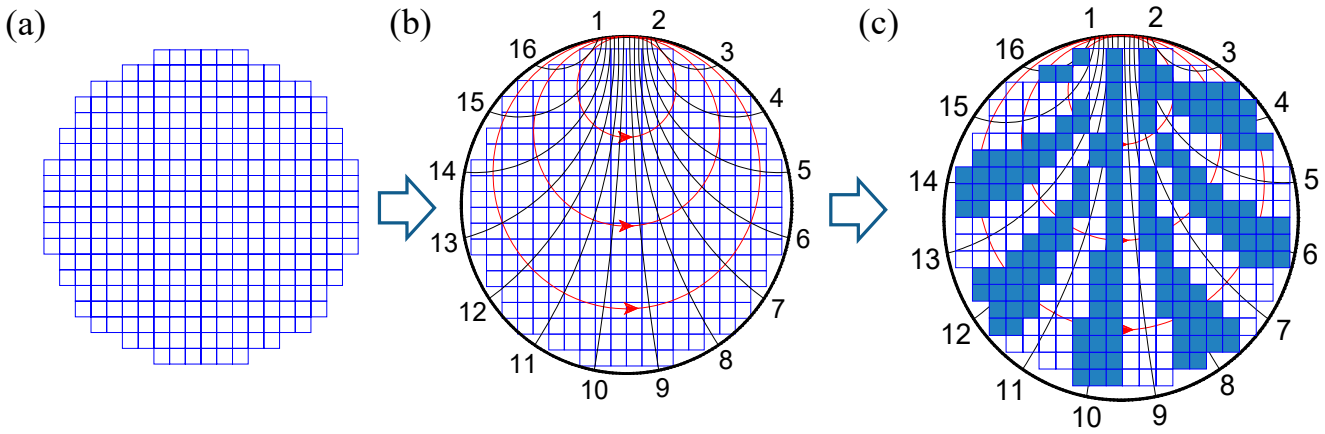


Figure 4. LBP method: (**a**) finite element, (**b**) potential isoline, (**c**) projection domain.

(1) When the contrast specimen was connected to the system, the calibration was carried out in order to determine the isometric line area corresponding to each element. The resistivity of all elements in the contrast specimen was equal; therefore, the positive problem of resistance tomography was calculated to obtain the potential of all nodes in

the sensitive field [4]. Since each electrode was the endpoint of each potential isoline, the potential in the sensitive field was equal to each electrode point, which was calculated with the finite element method, so as to draw the isostatic line in the corresponding sensitive field, as illustrated in Figure 4b.

(2) The isostatic line divides the sensitive field into several projection areas, and then the projection domain to which each element belongs can be determined. The real equipotential line, however, must pass through the elements. The approximate calculation of utilizing the potential at the element's center to represent the unit potential is inaccurate, but the computation may be substantially simplified. The calculating impact of this simplified technique fulfilled the application requirements, as evidenced by the simulated trial results. When the electrode pair 1–2 was the excitation electrode, the contour projection domain distribution in the sensitive field was as shown in Figure 4c.

(3) The modeled concrete specimen was connected to the system, and the boundary voltage was measured, as shown in Table 4.

Table 4. Voltage measurement of the contrast sample.

Electrode Pair	Electrode Pair for Voltage Measurement/mV														
	1–2	**2–3**	**3–4**	**4–5**	**5–6**	**6–7**	**7–8**	**8–9**	**9–10**	**10–11**	**11–12**	**12–13**	**13–14**	**14–15**	**15–16**
16–1		1557	951.4	415.5	229.9	168.3	145.1	142.2	156.6	168.5	296.8	677.2	1112	1948	
1–2			2139	969.0	469.1	294.4	190.3	139.5	159.9	167.2	193.5	290.5	588.6	863.5	1879
2–3				1678	775.6	404.5	306.3	220.6	170.4	167.9	169.0	248.9	381.1	761.6	1271
3–4					1990	962.4	495.9	346.3	254.4	214.6	174.0	211.4	262.1	379.9	730.7
4–5						1918	889.9	574.2	412.9	327.4	214.2	182.5	162.8	154.1	456.8
5–6							1779	989.9	661.8	349.0	268.2	203.6	154.1	151.2	398.8
6–7								1933	943.8	583.3	461.6	329.3	220.5	179.8	149.4
7–8									1655	758.0	521.5	385.2	298.8	231.4	182.5
8–9										1855	922.9	622.2	462.8	367.9	310.5
9–10											1944	936.1	598.6	436.3	354.6
10–11												1905	876.7	518.8	379.8
11–12													2076	863.5	515.4
12–13														1800	751.4
13–14															1582
14–15															
15–16															

(4) The distribution of the isostatic lines in the field was considered mostly unchanged, then when the boundary measurement voltage changed from V_i to V_i', the average resistivity in the corresponding projection domain was set according to formula (1). Therefore, for each element, all the resistivities, corresponding to every excitation current, were linearly superposed so as to obtain the resistivity of each element. The resulting resistivity distribution field was a grayscale pixel image, and then the resistivity distribution or conductivity distribution of the gradient distribution was obtained with the interpolation algorithm, as shown in Figure 5.

$$\frac{\rho_i'}{\rho_i} = \frac{V_i'}{V_i} \tag{1}$$

where ρ_i is the resistivity of the element of the contrast specimen in the "i"th measurement, ρ_i' is the resistivity of the element of the detecting specimen in the "i"th measurement, V_i is the voltage of the contrast specimen in the "i"th measurement, and V_i' is the voltage of the detecting specimen in the "i"th measurement.

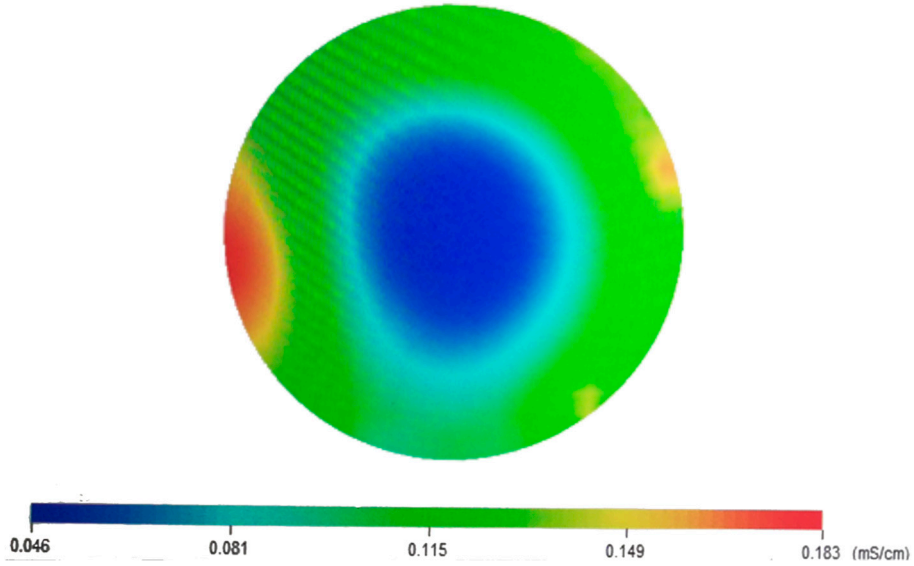


Figure 5. Conductivity image tomography.

The above process shows that a sensor member in excitation mode only needs to be calculated once. Such a reconstruction process does not need to inverse a large matrix; as a result, the calculation burden of the whole process is small, and the reconstruction speed is fast. When the variation between the nonuniform resistivity distribution and the uniform resistivity distribution is small, the image reconstruction error is also smaller and acceptable. For detecting the inclusive aggregates whose resistance is different from the surrounding mortar within a reasonable region in concrete, the LBP method is suitable.

3.2. Conductivity Image Tomography and Discussion

This test yielded a total of 104 voltage readings, the precise values of which are displayed in Table 4 for the contrast sample and in Table 5 for the modeled concrete sample. In Table 4, the minimum voltage is 142.2 millivolts, the maximum voltage is 2139 millivolts, and the average voltage is 654.3 millivolts. In Table 5, the minimum voltage is 204.6 millivolts, the maximum voltage is 1548 millivolts, and the average voltage is 537.6 millivolts. The overall resistivity of the modeled concrete was greater due to the inclusive stone's greater resistivity; therefore, the average voltage of the modeled concrete was smaller than that of the contrast. When the current was applied to 16–1, the potential differences of 14 independent adjacent electrode pairs were obtained. It shows that the potential difference of the electrode pair adjacent to 16 and 1 was greater, and that away from 16 and 1, it was smaller, which conforms to the law of equipotential lines. According to the statistics of all the voltage measurements, the voltage measurement value closer to the current exciting electrode pair was greater. The voltage value decreased rapidly as the distance increased. The voltage measurement value farther from the current exciting electrode pair was essentially stable.

This experiment used the LBP method to rebuild conductivity images, and the results are presented in Figure 5, which clearly illustrates the visual measuring impact of ERT. Note that the conductivity and resistivity are reciprocal. By comparing the conductivity picture to the real specimen, we can observe that the green region around the resistivity image is the conductive mortar, with a conductivity of 0.115 ms/cm. The natural aggregate is in the dark blue region, and the conductivity is 0.046 ms/cm. Furthermore, the light blue transition between the dark blue and green areas correlates to the interfacial transition zone (ITZ), whose conductivity is about 0.081 ms/cm. The photos indicate that resistivity imaging of concrete using ERT can directly display the distribution of natural aggregate and ITZ in concrete, assisting us in understanding the internal condition of concrete. This indicates that ERT is a suitable method for reflecting the various types of materials in

concrete; therefore, ERT can be used to detect the content of low-conductivity natural aggregates with low conductivity and, furthermore, the content of recycled aggregate, which has relatively high conductivity.

Table 5. Voltage measurement of the modeled concrete.

Electrode Pair	Electrode Pair for Voltage Measurement/mV														
	1–2	**2–3**	**3–4**	**4–5**	**5–6**	**6–7**	**7–8**	**8–9**	**9–10**	**10–11**	**11–12**	**12–13**	**13–14**	**14–15**	**15–16**
16–1		1079	556.6	426.3	355.5	287.6	233.4	204.6	219.7	228.5	293.9	353.5	527.3	1147	
1–2			1362	717.8	495.6	366.2	289.1	251.5	266.6	272.0	335.9	363.3	436.0	639.6	1318
2–3				1465	722.7	447.8	323.2	267.1	274.4	272.5	325.2	332.5	356.4	416.0	571.3
3–4					1548	712.9	441.4	330.6	321.8	307.1	351.1	341.8	342.3	355.5	393.1
4–5						1421	659.2	425.3	379.9	346.2	380.9	357.4	342.8	336.4	338.4
5–6							1392	659.2	490.2	406.7	420.9	373.0	336.4	312.0	295.4
6–7								1284	625.0	432.1	416.0	355.0	311.5	281.3	258.8
7–8									1226	561.5	460.4	359.4	295.4	252.9	224.1
8–9										1152	683.6	460.9	342.8	272.5	230.0
9–10											1440	693.4	443.4	323.2	262.7
10–11												1411	649.4	384.3	281.3
11–12													1538	639.6	381.8
12–13														1333	556.6
13–14															1172
14–15															
15–16															

The red region on the left edge in Figure 5 was caused by the conductive concrete and mold wall being slightly separated throughout the specimen preparation procedure, which was determined by examining and comparing the aggregate and conductive mortar specimens. According to this, the initial crack distribution of the shrinkage or loading of concrete may be found with the ERT method. Together with a measurement of the conductivity threshold of different crack conditions, ERT allows researchers to investigate the initial distribution of internal cracks and concrete damage.

4. Discussion

Although electrical resistivity tomography technology originates from medical research, it still has broad development prospects in engineering applications and can be widely used in the industrial, biological, and medical fields. It is a feasible way to use resistance tomography to reconstruct an image of concrete, study its initial damage distribution characteristics, and explore and grasp the damage evolution law in different kinds of concrete. Resistance tomography is a nondestructive testing method that is noninvasive, fast, low-cost, intuitive, and easy to analyze, making it suitable for long-term online monitoring [7]. As an electrical parameter tomography measurement technology, resistance tomography not only has the acquisition speed block and the low cost of general electrical parameter tomography measurement technology: it also has strong noise resistance and does not need to consider current phase transformation, different from capacitance tomography technology. However, since resistance tomography is an image reconstruction method for the pathological inverse problem, it can be considered to solve the inverse problem algorithmically [15].

It should be mentioned that conductive fillers, especially nano-conductive fillers, in concrete could exaggerate the accuracy of ERT [24]. This is because the contact resistance between the electrode and the matrix is not negligible; when the resistivity of the matrix is low, the contact resistance can also be effectively reduced; and the influence of the

contact resistance on the accuracy of ERT can be reduced. In addition, the moisture in the matrix creates inhomogeneity [26]. In this study, the specimen was stored in air for more than two months, so the humidity content in the test block was low and stable. The test blocks were stored in the natural environment for two months in order to simulate the moisture content of ordinary concrete and to find a way to test the distribution of aggregate inclusions and ITZ in ordinary concrete. As the change in conductivity of the concrete containing graphene due to damage was more prominent than the effects of moisture, the ERT method was able to capture the damage-induced conductivity changes. For instance, the ITZ always showed lower conductivity because of the lower conductive filler content. The effects of moisture on the ERT analysis will be investigated in future studies.

As compared to visual inspections, the ERT method does not only detect surface cracks. The detection range of ERT varies with the range of electrode arrangements and can even be used in the entire concrete project, whether it is a road or a dam, which creates opportunities for a wider range of applications in engineering.

5. Conclusions

(1) This paper investigated the link between the location distribution of current-stimulated electrodes and the number of independent voltage measurements. The number of effective voltage measurements of 16 electrodes in the neighboring excitation mode was calculated, and all real voltage measurements were counted systematically. The voltage measurement values closer to the current exciting electrode pair were greater and decreased rapidly as the distance increased.

(2) Based on the electrical resistivity image reconstruction of the aggregate and graphene mortar, it was found that ERT can reflect the locations of aggregate, ITZ, and cracks in concrete. Natural aggregate and mortar have conductivities of 0.046 ms/cm and 0.115 ms/cm, respectively. The conductivity of the ITZ, which is always regarded as the initial damage, is about 0.081 ms/cm.

(3) This study demonstrates that ERT is able to investigate the interior conditions and initial damage of concrete. To do this, the shape, orientation, and resistance of the inclusive aggregate need to be considered as changing parameters to make the study more comprehensive. Because the conductivity of the mortar and aggregate varies, a potential technique for determining whether recycled aggregate is used in fresh concrete may be constructed by comparing the resistivity threshold range of the mortar in ERT.

(4) This study used simplified two-dimensional concrete. In order to promote the application of ERT in real concrete structures, ERT research on real aggregates needs to be carried out in the future. In addition, this study mainly focused on the initial damage, which is the static damage. The damage evolution detection with ERT during curing or when the specimen is being loaded can be conducted in future research.

Author Contributions: Conceptualization, Q.L. and S.W.; methodology, Q.L.; formal analysis, S.W.; investigation, S.W. and W.L.; resources, S.W.; data curation, S.W.; visualization, S.P.; writing—original draft preparation, Q.L. and S.W.; writing—review and editing, Q.L., S.P. and W.L.; supervision, Q.L.; project administration, Q.L.; funding acquisition, S.W. All authors have read and agreed to the published version of the manuscript.

Funding: This work was financially supported by the Gansu Province Youth Science Foundation (20JR5RA079) Research Project of the State Grid Gansu Electric Power Corporation (52273019000B).

Data Availability Statement: The original contributions presented in the study are included in the article, further inquiries can be directed to the corresponding authors.

Conflicts of Interest: Authors Shijun Wang, Shengjiang Peng and Wanwei Li were employed by the company Gansu Electric Power Corp., State Grid. The remaining author declares that the research was conducted in the absence of any commercial or financial relationships that could be construed as a potential conflict of interest.

References

1. Azarsa, P.; Gupta, R. Electrical Resistivity of Concrete for Durability Evaluation: A Review. *Adv. Mater. Sci.* **2017**, *2017*, 8453095. [CrossRef]
2. Azhari, F.; Banthia, N. Cement-based sensors with carbon fibers and carbon nanotubes for piezoresistive sensing. *Cem. Concr. Compos.* **2012**, *34*, 866–873. [CrossRef]
3. Chen, P.; Chung, D.D.L. Concrete as a new strain/stress sensor. *Compos. B Eng.* **1996**, *27*, 11–23. [CrossRef]
4. Cuong, L.P.; Van Tho, L.; Juzsakova, T.; Rédey, Á.; Hai, H. Imaging the movement of toxic pollutants with 2D electrical resistivity tomography (ERT) in the geological environment of the Hoa Khanh Industrial Park, Da Nang. *Vietnam. Environ. Earth. Sci.* **2016**, *75*, 286. [CrossRef]
5. Hallaji, M.; Pour-Ghaz, M. A new sensing skin for qualitative damage detection in concrete elements: Rapid difference imaging with electrical resistance tomography. *NDT E Int.* **2014**, *68*, 12–21. [CrossRef]
6. Han, B.; Ding, S. Intrinsic self-sensing concrete and structures: A review. *Measurement* **2015**, *59*, 110–128. [CrossRef]
7. Han, B.; Yu, X.; Ou, J. Piezoresistive Characteristic Model of Nickel/Cement Composites Based on Field Emission Effect and Inter-Particle Separation. *Sens. Lett.* **2009**, *7*, 1044–1050. [CrossRef]
8. Han, B.; Yu, X.; Ou, J. Effect of water content on the piezoresistivity of MWNT/cement composites. *J. Mater. Sci.* **2010**, *45*, 3714–3719. [CrossRef]
9. Karhunen, K.; Seppänen, A.; Lehikoinen, A.; Monteiro, P.J.; Kaipio, J.P. Electrical Resistance Tomography imaging of concrete. *Cem. Concr. Res.* **2010**, *40*, 137–145. [CrossRef]
10. Kazakis, N.; Pavlou, A.; Vargemezis, G.; Voudouris, K.S.; Soulios, G.; Pliakas, F.; Tsokas, G. Seawater intrusion mapping using electrical resistivity tomography and hydrochemical data. An application in the coastal area of eastern Thermaikos Gulf, Greece. *Sci. Total Environ.* **2016**, *543*, 373–387. [CrossRef]
11. Konsta-Gdoutos, M.; Chrysoula, A. Self sensing carbon nanotube (CNT) and nanofiber (CNF) cementitious composites for real time damage assessment in smart structures. *Cem. Concr. Compos.* **2014**, *53*, 162–169. [CrossRef]
12. Lataste, J.F.; De Larrard, T.; Benboudjema, F.; Semenadisse, J. Study of electrical resistivity: Variability assessment on two concretes: Protocol study in laboratory and assessment on site. *Eur. J. Environ. Civ. Eng.* **2012**, *16*, 298–310. [CrossRef]
13. Liu, Q.; Wu, W.; Xiao, J.; Tian, Y.; Chen, J.; Singh, A. Correlation between damage evolution and resistivity reaction of concrete in-filled with graphene nanoplatelets. *Constr. Build. Mater.* **2019**, *208*, 482–491. [CrossRef]
14. Liu, Q.; Xu, Q.; Yu, Q.; Gao, R.; Tong, T. Experimental investigation on mechanical and piezoresistive properties of cementitious materials containing graphene and graphene oxide nanoplatelets. *Constr. Build. Mater.* **2016**, *127*, 565–576. [CrossRef]
15. de Castro Martins, T.; Sato, A.K.; de Moura, F.S.; de Camargo, E.D.L.B.; Silva, O.L.; Santos, T.B.R.; Zhao, Z.; Möeller, K.; Amato, M.B.P.; Mueller, J.L.; et al. A review of electrical impedance tomography in lung applications: Theory and algorithms for absolute images. *Annu. Rev. Control.* **2019**, *48*, 442–471. [CrossRef] [PubMed]
16. McKee, S.L.; Williams, R.A.; Boxman, A. Development of solid-liquid mixing models using tomographic techniques. *Chem. Eng. J. Biochem. Eng.* **1995**, *56*, 101–107. [CrossRef]
17. Priou, J.; Lecieux, Y.; Chevreuil, M.; Gaillard, V.; Lupi, C.; Leduc, D.; Rozière, E.; Guyard, R.; Schoefs, F. In situ DC electrical resistivity mapping performed in a reinforced concrete wharf using embedded sensors. *Constr. Build. Mater.* **2019**, *211*, 244–260. [CrossRef]
18. Rodrigues, R.; Gaboreau, S.; Gance, J.; Ignatiadis, I.; Betelu, S. Reinforced concrete structures: A review of corrosion mechanisms and advances in electrical methods for corrosion monitoring. *Constr. Build. Mater.* **2021**, *269*, 121240. [CrossRef]
19. Hallaji, M.; Seppänen, A.; Pour-Ghaz, M. Electrical resistance tomography to monitor unsaturated moisture flow in cementitious materials. *Cem. Concr. Res.* **2015**, *69*, 10–18. [CrossRef]
20. Xiao, H.; Li, H.; Ou, J. Modeling of piezoresistivity of carbon black filled cement-based composites under multi-axial strain. *Sens. Actuator A Phys.* **2010**, *160*, 87–93. [CrossRef]
21. Xu, J.; Zhong, W.; Yao, W. Modeling of conductivity in carbon fiber-reinforced cement-based composite. *J. Mater. Sci.* **2010**, *45*, 3538–3546. [CrossRef]
22. Yang, W.Q.; Spink, D.M.; York, T.A.; Mccann, H. Effect of Progesterone Receptor Blockade on Renin Synthesis and Secretion from Endometrial Stromal Cells: Pulse Experiment. *Am. J. Obstet. Gynec.* **1999**, *166*, 294.
23. Zhou, Z.; Liu, W.; Huang, Y.; Wang, H.; He, J.; Huang, M.; Ou, J. Optical fiber Bragg grating sensor assembly for 3D strain monitoring and its case study in highway pavement. *Mech. Syst. Signal Process* **2012**, *28*, 36–49.
24. Yoon, S.; Kim, M.K.; Kim, T.U.; Jeon, D.; Song, H.; Suh, J.-I.; Oh, J.E.; Kim, D.J. Enhancing image resolution in single-side electrical resistance tomography (ERT) by utilizing theoretical sensitivity analysis: Experimental validation and application to cement mortar. *J. Build.* **2024**, *84*, 108480.
25. Gupta, S.; Lin, Y.; Lee, H. In situ crack mapping of large-scale self-sensing concrete pavements using electrical resistance tomography. *Cem. Concr. Compos.* **2021**, *122*, 104154.
26. Jeon, D.; Kim, M.K.; Jeong, Y.; Oh, J.E.; Moon, J.; Kim, D.J.; Yoon, S. High-accuracy rebar position detection using deep learning–based frequency-difference electrical resistance tomography. *Autom. Constr.* **2022**, *135*, 104116.
27. Movahedi, S.; Taghizadieh, N. Efficiency improvement of radial basis function meshless method in conjunction with bayesian theorem for electrical tomography of heterogeneous concrete. *Eng. Anal Bound Elem.* **2022**, *135*, 382–393.

28. Dalton, L.E.; Räsänen, M.; Voss, A.; Seppänen, A.; Pourghaz, M. Investigating the use of electrical capacitance tomography to image rapid transient moisture flow through cracks in concrete. *Cem. Concr. Compos.* **2023**, *140*, 105070. [CrossRef]
29. Achrafi MK, E.; Bonnet, S.; Villain, G. Electrical resistivity tomography results analyzed with two inversion methods to determine chloride profiles on BFS concrete having very high electrical resistivity. *Constr. Build. Mater.* **2023**, *407*, 133361. [CrossRef]
30. *GB 175-2020*; Common Portland Cement. Chinese National Standards: Beijing, China, 2020. (In Chinese)

Disclaimer/Publisher's Note: The statements, opinions and data contained in all publications are solely those of the individual author(s) and contributor(s) and not of MDPI and/or the editor(s). MDPI and/or the editor(s) disclaim responsibility for any injury to people or property resulting from any ideas, methods, instructions or products referred to in the content.